

Introducing a data-driven framework for spatiotemporal slope stability analytics for failure estimation

A Tordesillas *The University of Melbourne, Australia*

S Kahagalage *The University of Melbourne, Australia*

L Campbell *GroundProbe, Australia*

P Bellett *GroundProbe, Australia*

R Batterham *The University of Melbourne, Australia*

Abstract

In this paper, we present spatiotemporal slope stability analytics for failure estimation (SSSAFE), a deterministic, data-driven model of force transmission in a rock slope. Its input solely comprises the spatiotemporal surface deformation of the slope, here gathered from slope stability radar (SSR). The model combines recent advances from data analytics, granular media physics and mechanics, and slope stability monitoring. SSSAFE is unique in its explicit connections to the underlying physics of strength and failure in the precursory failure regime (PFR) of granular systems. Distinct from the single pixel selection for time of failure methods, this model exploits all the kinematic information available on the entire monitoring domain to quantitatively track the coupled evolution of the preferred transmission pathways for force and energy (so-called force chains) and the preferential crack paths. This coupled evolution gives rise to a force bottleneck, which comprises vulnerable and congested sites closest to breaking point (fracture).

The force bottleneck is an emergent structure that is not static. Prior studies have shown that the spatiotemporal dynamics of this bottleneck holds clues to the ultimate location and timing of failure. Initially, in the early stages of PFR, the bottleneck continually shifts in location in the rock body. This process is due to the inherent redundancies in the force pathways in the rock mass. Such redundant paths enable stresses to be redistributed and diverted away from the pre-existing bottleneck to another location where a new bottleneck may then form. However, as damage spreads, and the time of failure draws near, a tipping point is reached when all the redundant paths have been exhausted and no further stress reroutes are possible. At this point, a recurring bottleneck, invariant in space and time, emerges along which previously disconnected cracks begin to coalesce. Simultaneously, this process leads to a persistent kinematic clustering pattern, as the active region begins to detach from the rest of the slope and accelerate. That is, the closer it is to the time of failure, the more the kinematic clusters (the two groups of monitoring points on either side of the bottleneck) move such that intra-cluster motions become increasingly similar while inter-cluster motions become increasingly different. Here we demonstrate how to extract, quantify, and exploit this particular form of spatiotemporal dynamics from SSR data for two distinct open pit mine slopes, for the purposes of early prediction of failure of the geometry, location, and time of collapse.

Keywords: *slope stability analytics, force bottlenecks, spatiotemporal dynamics, force chains*

1 Introduction

Significant recent advances in the fundamentals of granular media failure present game changing opportunities for synergy through integration of the state-of-the-art in three areas: slope stability monitoring (Dick et al. 2015; Carlà et al. 2016; Intrieri et al. 2019; Saunders et al. 2020), physics and mechanics of granular media (Tordesillas et al. 2015a, 2016, 2020a, 2020b), and spatiotemporal data analytics (Wang et al. 2020). Slope monitoring using SSR systems is widely adopted in the mining industry, delivering large quantities of displacement (and velocity) data to operators (Dick et al. 2015; Saunders et al. 2020). While various

techniques are used to programmatically warn of impending collapse, the state-of-the-art in forecasting a collapse remains the inverse velocity method (Fukuzono 1985; Harries et al. 2006; Carlà et al. 2016). This method is proven and robust, but it requires an operator to fit many linear regressions to the data as the failure progresses. Moreover, it does not incorporate any spatial information (Dick et al. 2015; Carlà et al. 2019) owing to the complexities of incorporating both temporal and spatial correlations in multivariate time series data analysis (Wang et al. 2020). This limitation has implications for robust early prediction of failure in granular systems (i.e. assemblies of a large number of discrete grains).

High resolution experiments on granular materials—spanning ductile to quasi-brittle deformation—have shown that the precursory evolution of failure is inherently spatiotemporal (Tordesillas et al. 2012, 2013b, 2015a, 2016, 2020a, 2020b). Of crucial benefit to slope stability monitoring is that such precursory events manifest spatiotemporal deformation patterns that are indicative of the location and timing of impending failure. Recent studies, from laboratory-scale to field-scale studies, have also shown that such patterns provide reliable clues to the ultimate failure location Ω early in the PFR; refer to, for example, Tordesillas et al. (2021a), Das & Tordesillas (2019), and Singh & Tordesillas (2020). These clues can be exploited for control and management of slope failure hazards, in the same way that such precursory signatures have been used to shape and direct the course of failure to achieve specific target behaviour in granular systems (Tordesillas 2018).

In this paper, we introduce a novel data-driven framework for spatiotemporal slope stability analytics for failure estimation (SSSAFE). Using SSR deformation data, we employ SSSAFE to characterise the spatiotemporal dynamics of force transmission in a monitored rock slope for the purposes of predicting where and when a collapse will likely occur. The case studies are both from an open pit mine, and are referred to here as Mine 1 and Mine 2. Mine 1 is a circular failure on a waste spoil pile with a complex deformation time series (progressive to regressive trends (Sullivan 2007), while Mine 2 is a structurally controlled failure in intact hard rock with a classic exponential deformation time series. The rest of the paper is arranged as follows. We first describe the method behind SSSAFE in Section 2. Next, we present each case study and the results from SSSAFE in Section 3. A discussion of the scope and limitation of SSSAFE is given in Section 4 before a brief conclusion in Section 5.

2 Method

SSSAFE is a deterministic, data-driven model of the transmission of force in a rock body that depends on kinematic information for its input; here ground surface deformation (displacement) in the radar line-of-sight direction. It is unique because of its explicit connections to the underlying physics of strength and failure in granular media (Tordesillas et al. 2020b) and the theory of fracture mechanics (Tordesillas et al. 2020a). In particular, SSSAFE is the outcome of a recent breakthrough in which Griffith's theory for crack propagation was extended to complex, heterogeneous and disordered quasi-brittle materials through a model of the transmission of force (and energy) in a space-time evolving network representation of the body. This model is designed to use all the kinematic information from the entire monitoring domain to quantitatively track the coupled evolution of the preferred transmission pathways for force and energy (so-called force chains) and the preferential crack paths.

SSSAFE proceeds in three steps, as illustrated in Figure 1.

Step 1 is the abstraction of the kinematic data, and representation of the rock body, into a two-dimensional surface flow network \mathcal{F} that transmits force or energy (Tordesillas et al. 2020a, 2020b). Since force transfer occurs along physical connections, the links of \mathcal{F} represent the physical connectivity of the body. For example, in a laboratory sample, the nodes of \mathcal{F} represent the grains while the links of \mathcal{F} are the grain-grain contacts. In the gridded monitoring data from SSR, the nodes of \mathcal{F} are the pixels while the links of \mathcal{F} are decided using various connection rules. One simple rule is to connect monitoring points in close proximity (e.g. grid pixels which share a common boundary (Figures 1a and 1b)). The resultant \mathcal{F} is called a proximity network. Each link in \mathcal{F} , denoted by e , is weighted with a prescribed capacity \mathcal{M}_e which reflects the local 'bond strength' between connected parts of the rock mass. A force flow along link e , x_e , is non-negative and

cannot exceed the link capacity: $0 \leq x_e \leq \mathcal{M}_e$. In other words, \mathcal{M}_e is the force that must be overcome to break apart the material connection (or disconnect the corresponding link e in \mathcal{F}). In Tordesillas et al. (2021a), the link capacity \mathcal{M}_e is expressed in terms of the relative displacement of the associated pixel locations:

$$\mathcal{M}_e = \frac{1}{|\Delta u_e|^2} \quad (1)$$

where $|\Delta u_e|$ is the magnitude of the relative displacement of the pixels/nodes connected by link e . Thus, the weaker the bond strength (the lower the \mathcal{M}_e), the higher the relative motion in the corresponding pixel locations on the slope. Since the grid is fixed over the course of the monitoring campaign, the construction of \mathcal{F} is performed once at the start of the monitoring campaign; albeit its link capacities which reflect the changing slope deformation naturally change as time advances.

Step 2 is a dual optimisation problem on the flow network \mathcal{F} , solved at every time stage of the monitoring campaign; the solution to which identifies the preferred pathways for force and damage (Figures 1c–1e). We refer readers to Tordesillas et al. (2021a) for complete details of this optimisation process. Here, we focus solely on a key output solution which is the force bottleneck β – the path of least resistance to fracture.

The bottleneck distinguishes itself by having the least capacity out of all the *feasible fracture paths in the body* (the minimum cuts of the flow network \mathcal{F}): see the illustration in Figure 1. A path or cut ℓ of \mathcal{F} is a set of links in \mathcal{F} which, if disconnected, represents a literal cut of \mathcal{F} into two disjoint components such that no flow can be transmitted from the source node q to the sink node k . The capacity or resistance to fracture of such a path $R(\ell)$ is thus the sum of the capacity of the links in ℓ and is given by:

$$R(\ell) = \sum_{e \in \ell} \mathcal{M}_e. \quad (2)$$

The capacity of the force bottleneck, denoted by $R^* = R(\beta)$, is the failure resistance of the slope. R^* is equal to the maximum flow (the maximum amount of force flow that can be transmitted through \mathcal{F}) by the well-known maximum-flow minimum-cut theorem (Ahuja et al. 1993). The failure resistance is given by:

$$R^* = \min_{\ell \in \mathcal{F}} R(\ell) = \sum_{e \in \beta} \mathcal{M}_e. \quad (3)$$

The force bottleneck is a dynamic structure. More importantly, recent studies have shown that its spatiotemporal dynamics in the PFR holds clues to the location and timing of an impending failure (Das & Tordesillas 2019; Singh & Tordesillas 2020; Wang et al. 2020; Zhou et al. 2021; Tordesillas et al. 2021a). In the early stages of PFR, the force bottleneck is highly transient. This is because a relatively stable granular body is a redundant structure. Such a body has many redundant force pathways available to accommodate stress reconfigurations that relieve stress build-up in—and divert damage away from—vulnerable bottleneck sites. In turn, this process has the effect of shifting the bottleneck location.

As damage spreads and the time of failure draws near, redundancies in transmission pathways diminish until such time when all alternative paths that can accommodate rerouted forces are exhausted. At this point, a regime change point t^* is reached from when damage can no longer be avoided in the pre-existing bottleneck, thus making links along this path highly predisposed to cascading failure. From t^* , the bottleneck essentially persists in the same location through time; we call this the recurring bottleneck \mathcal{B} . As shown in prior studies, from t^* , previously disconnected cracks begin to propagate and coalesce along \mathcal{B} (Tordesillas et al. 2020a, 2020b). Simultaneously, while the material connections along \mathcal{B} break apart, the region of impending failure becomes increasingly detached from the rest of the slope. Pixels in the active region begin to distinguish themselves by moving as a coherent whole (in near rigid-body motion) at increasingly higher velocities than those of the pixels in the stable zone.

The above pattern of ground motion that ensues on either side of \mathcal{B} manifests as a clustering pattern ζ when studied in the state-space of displacements (Tordesillas et al. 2021a). That is, two groups of monitoring points emerge: the active or fast-moving cluster (denoted by ζ_A) which we previously found to reliably predict the failure region Ω versus the rest of the slope. We exploit this pattern in Step 3.

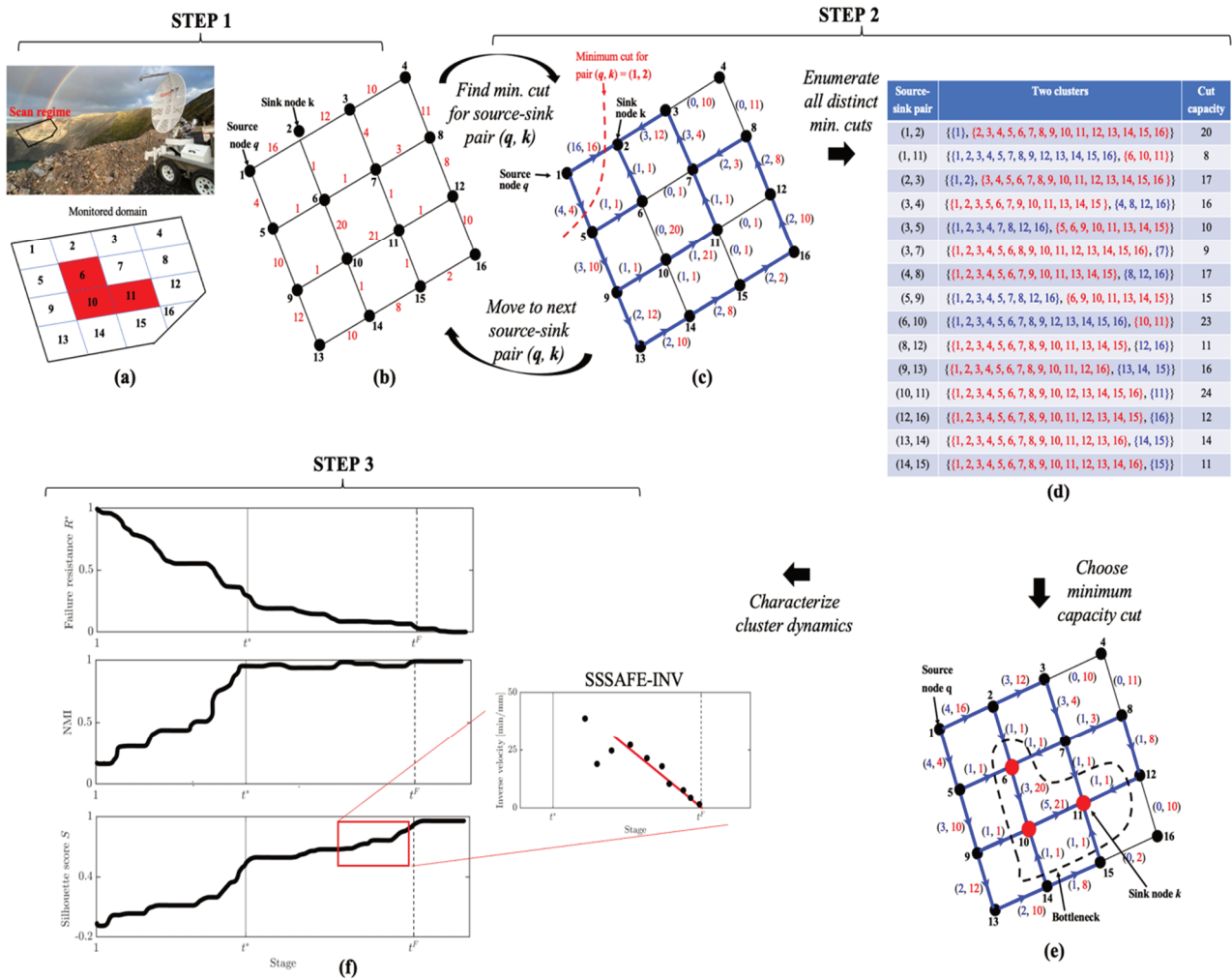


Figure 1 SSSAFE proceeds in three steps. Step 1: (a) Zoomed-in view of the monitored domain split into 16 pixel locations with the failure region highlighted in red; (b) A flow network is constructed to represent the slope. Link labels are in the form (x_e, \mathcal{M}_e) : x_e and \mathcal{M}_e denote, respectively, the flow and capacity of link e , both of which depend on the SSR-measured deformation. Step 2: (c) The maximum-flow minimum-cut problem is solved for all possible source-sink pairs. The minimum cut between nodes 1 (source node q) and 2 (sink node k) is shown (red dashed line); (d) Information on all distinct minimum cuts is enumerated; (e) The bottleneck is found from the minimum cut, the cut with the global minimum capacity: the cut corresponding to the source node $q = 1$ and the sink node $k = 11$. The failure resistance of the slope is thus $R^* = 8$. Removal of links in the bottleneck yields a pair of kinematics clusters. The active cluster ζ_A (red nodes) is that with the higher mean velocity of the two clusters on either side of \mathcal{B} . The corresponding maximum flow paths solution yields the preferred paths for force transmission (blue links). Step 3: (f) Dynamics of the kinematic clusters, quantified from the evolution with time of R^* , NMI and S , is used to determine the regime change point t^* . For brevity of illustration, we assume that $t \geq t^*$ such that the bottleneck found from Step 2 is the recurring bottleneck \mathcal{B} (dashed black line). The active cluster ζ_A is used to predict the region of impending failure Ω . SSSAFE-INV analysis performed on ζ_A yields the time of failure t^F

Step 3 characterises the spatiotemporal dynamics of the kinematic clusters delimited by β to determine the regime change point t^* and the likely location of the impending failure region Ω for $t \geq t^*$. Cluster dynamics are quantified by computing the Silhouette score S (Rousseeuw 1987) coupled with an information-theoretic measure of normalised mutual information (NMI) (Vinh et al. 2010).

The Silhouette score $S \in [-1, 1]$ gives an overall measure of the quality of clustering (Rousseeuw 1987) by quantifying the extent to which intra-cluster motions become increasingly similar as inter-cluster motions become increasingly different from each other in displacement state-space. It is the global average of $s(j)$ which measures how similar a given node j is to the other nodes i in its own cluster (cohesion) compared to the nodes in the other clusters (separation):

$$S = \frac{1}{n} \sum_{j=1}^n s(j) = \frac{1}{n} \sum_{j=1}^n \frac{b(j) - a(j)}{\max[a(j), b(j)]} \quad (4)$$

where $a(j)$ is the average distance in the displacement state-space from j to all other nodes in the same cluster, and $b(j)$ is the average of the distances from j to all points in the other cluster. A good clustering pattern (high S) is one where the nodes in the same cluster exhibit very similar features (nodes are tightly packed in feature state-space, hence small $a(j)$); while nodes from different clusters have very different features. As a general guide, values below 0.2 suggest essentially no clustering pattern was found, while the closer S is to 1, the more compact are the individual clusters while being more separated from each other. Given the studied feature is motion, an increasing trend with respect to time in S from around 0.2 to its upper bound of 1 suggests that the clusters are moving in increasingly relative rigid-body motion.

The NMI determines whether the pattern of impending failure has become physically incised in the slope (Tordesillas et al. 2021a), by measuring the cluster similarity at two consecutive time states. NMI is defined as:

$$\text{NMI} = \frac{I(\zeta^t; \zeta^{t-1})}{\sqrt{H(\zeta^t)H(\zeta^{t-1})}} \quad (5)$$

where $I(\zeta^t; \zeta^{t-1})$ is the mutual information between the clustering pattern at the current time ζ^t and that at the previous time ζ^{t-1} and $H(\cdot)$ is the entropy of the corresponding clustering assignments. $\text{NMI} \in [0, 1]$: 0 means there is no mutual information, as opposed to 1 where there is perfect correlation or similarity, between ζ^t and ζ^{t-1} . Intuitively, NMI measures the information that the clustering assignments ζ^t and ζ^{t-1} share. Thus, the higher the NMI, the more useful information on the clustering pattern is encoded in ζ^{t-1} that can help predict the clustering at the next time state ζ^t .

To determine the regime change point t^* , we combine the information gathered from the failure resistance R^* , the Silhouette score S , and NMI (Figure 1f). Specifically, the regime change point t^* is the time from which the failure resistance R^* drops close to its minimum of 0, as S rises and/or levels above 0.2, while NMI stays close to 1. For all $t \geq t^*$, a prediction on the slope failure region is given by the active (fast-moving) cluster that is delimited by the recurring force bottleneck \mathcal{B} . If the monitoring commenced after t^* , such that the active cluster ζ_A becomes essentially invariant, then we can expect S to remain high above 0.2, while NMI stays close to 1. That means, even though no further regime change point may be detected over the studied time states, the temporal persistence of high values for both S and NMI serves as a good indicator of a high-risk area that is prone to failure.

For slopes exhibiting tertiary creep deformation, we propose the SSSAFE-INV (inverse velocity) analysis to predict the time of failure t^F (Figure 1f). This is achieved by performing a linear regression analysis, using a continuous and overlapping rolling time window, of the time evolution of the inverse mean velocity of ζ_A for $t \geq t^*$. Thus with respect to detecting the time of failure t^F , the main advance achieved here is that SSSAFE-INV not only obviates the need to subjectively select a pixel to implement the Fukuzono INV analysis (Fukuzono 1985) but also ensures SSSAFE-INV takes into account the spatiotemporal and coupled evolution of force and damage pathways in PFR.

3 Case studies

We tested the performance of SSSAFE in two mine slopes: Mine 1 and Mine 2. Mine 1 can be classified as a ductile failure, while Mine 2 is a brittle failure. The mine operation, location and year of the rockslides are confidential; however, all the information necessary for this analysis has been made available and is summarised in the following sections.

3.1 Mine 1

3.1.1 Background and data on Mine 1

Mine 1 is a waste spoil pile: a slope constructed from dumped loose rock, derived from blasted and/or excavated overburden (Figure 2a). The monitored domain measures around 200 m in length and 40 m in height. Movements of the rock face were monitored over a period of three weeks: 10:07 31 May to 23:55 21 June. Line-of-sight displacement at each observed location on the surface of the rock slope was recorded every six minutes, with millimetric accuracy. This led to time series data comprising 1,803 monitoring points. A rockslide of circular failure type, with an arcuate back scar and a strike length of around 120 m, occurred on the west wall of the slope at $t_1^F = 3,568 = 13:10$ 15 June reaching peak pixel velocity of around 640 m/yr. A sharp rise to a peak of 33.61 mm/h at t_1^F can be observed in the global mean velocity for the monitoring domain (Figure 2c). As can be observed in Figure 2e, the deformation time series exhibits complex progressive to regressive trends.

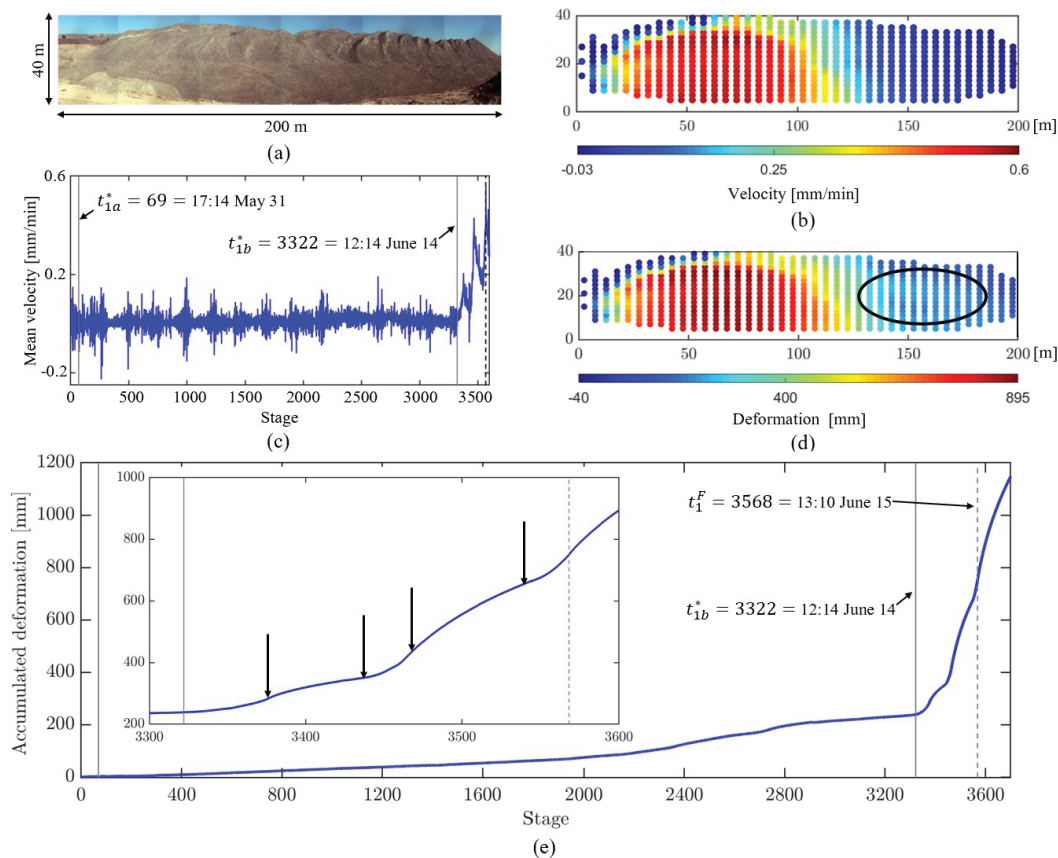


Figure 2 Mine 1: (a) The monitored domain; (b) Spatial map of velocity at time of failure; (c) Time evolution of global mean velocity; (d) Spatial map of accumulated displacement at time of failure. The second region of instability to the southeast corner (circled) did not lead to a collapse; (e) Deformation time series for pixel ϱ : pixel with the highest rate of movement in ζ_A at the time of failure. Zoomed-in view of the time period from 3,300 to 3,600 highlights the progressive and regressive phases of the deformation in the final stages after the second regime change point $t_{1b}^* = 12:14$ 14 June (vertical arrows indicate transition points from one phase to the next)

There is a ‘competing slide’ to the east (Figure 2d). This second site of instability developed large movements intermittently during PFR, but the instability was arrested, and movement slowed down the day before the collapse of the west wall. In this context, this region is sometimes referred to as a false alarm in the sense that it did not eventuate into a collapse. While in many cases ‘tertiary creep’ ends with a failure, it is also possible that the whole or part of the landslide finds a new equilibrium. One likely cause of this in the case

of Mine 1 is a reduction of the local destabilising forces through complex stress redistributions that ultimately slow down or arrest the whole or part of the landslide body. Details of these stress redistributions are discussed elsewhere (Tordesillas et al. 2020a, 2020b, 2021a).

3.1.2 Results on Mine 1

SSSAFE reliably identified and differentiated, in space and time, the two unstable zones in Mine 1. In space, the west wall, where catastrophic failure ultimately occurred, was distinguished early in PFR by the persistence of the predicted failure boundary (black pixels) in this area, in contrast to the eastern corner where this boundary only occasionally appeared (Figure 3a). In time, we observed two regime change points in PFR, t_{1a}^* and t_{1b}^* . To ease identification of these points, we present the failure resistance R^* in log scale (Figure 3b). The first regime change point is at around $t_{1a}^* = 69 = 17:14$ 31 May, when the drop in R^* coincides with a rise in both NMI and S (Figures 3c and 3d). As time advances from t_{1a}^* , there is an initial decline in the quality of clustering S while NMI stays close to 1. The former is due to the dynamic interaction between the two regions of instability (active clusters) while the latter is due to the persistence of the west wall belonging to the active cluster ζ_A (either in part or as the whole of ζ_A) from the early stages of the monitoring campaign. The second regime change point occurs at $t_{1b}^* = 3,322 = 12:14$ 14 June, the day before the collapse, when S sharply rises.

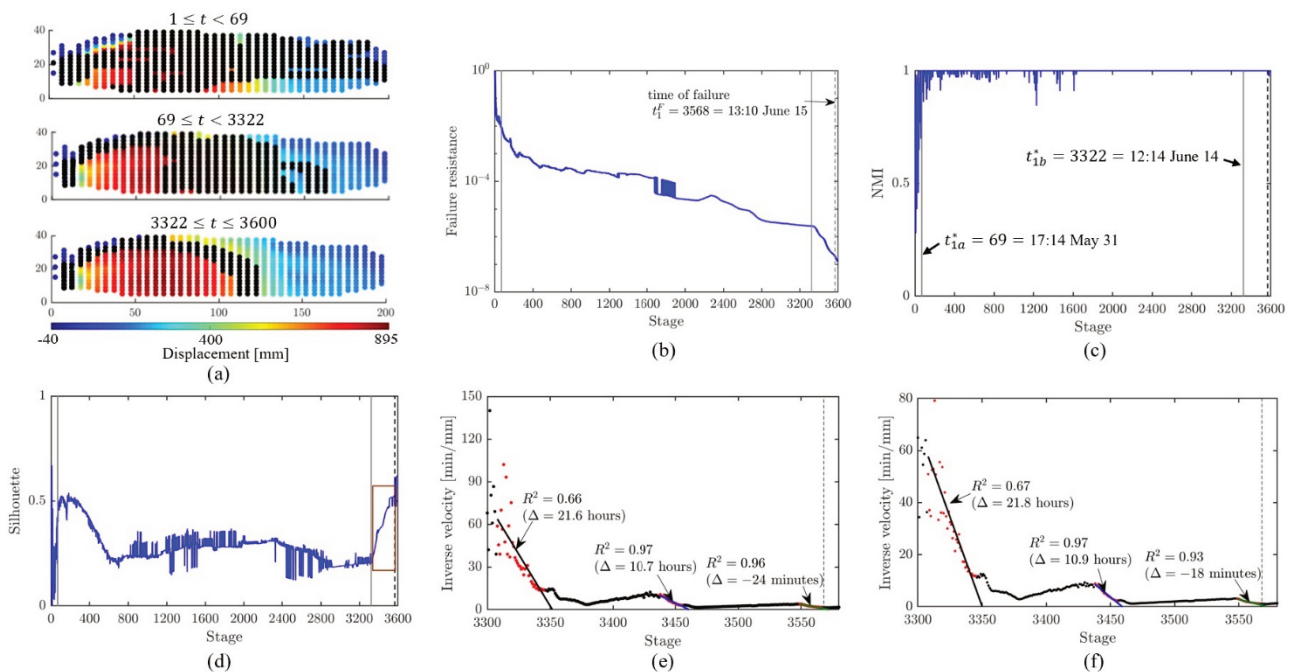


Figure 3 Mine 1: (a) Bottleneck sites across three distinct regimes. Time evolution of (b) failure resistance R^* in log scale; (c) NMI; (d) Silhouette S ; (e) Inverse mean velocity of ζ_{Ai} ; (f) Inverse velocity of ϕ . Vertical lines mark the regime change points (solid grey line) and the time of failure (dashed black line), respectively. Red rectangular outlines in (d) highlight the time period when SSSAFE-INV analysis was performed. Results of the SSSAFE-INV analysis in (e) and (f) show Δ , the actual time of failure t_1^F minus the predicted time of failure; and R^2 , the goodness-of-fit to the linear regression model

These trends can be explained from the viewpoint of the coupled evolution of force chains and preferred damage pathways (e.g. macrocracks, shear bands) (Tordesillas et al. 2015a, 2020a, 2020b). The drop in R^* at t_{1a}^* suggests that internal cracks and shear bands have started to propagate, as delineated by the force bottlenecks (black pixels in Figure 3a) which identify rock mass sites that are closest to fracture. In particular, damage spread, which likely initiated even before the time period covered by the data analysed here, is to the extent that the capacity for force transfer between connected material points (pixels) along the recurring bottleneck B to the west has significantly reduced as early as t_{1a}^* . Despite this degradation, the low values of

S over the subsequent time period $69 \leq t < 3,322$ suggest that there remain redundant force pathways in the slope mass to enable stress reconfigurations that relieve the build-up of stress in β . That is, alternative paths exist to which forces and damage can be diverted away from β —specifically, towards the competing slide to the east, as evident in the intermittent eastwards movement of bottleneck sites. This dynamic interaction between the two regions of instability continues until the day before the collapse, t_{1b}^* , from when S rises again. This final significant increase in S suggests that all redundant paths have been exhausted and no further stress reroutes away from \mathcal{B} can be accommodated. Thus \mathcal{B} is now poised for catastrophic failure. Previously disconnected microcracks propagate and coalesce along \mathcal{B} to form the rockslide boundary. Simultaneously, the clustering pattern becomes incised in the slope as the kinematic clusters undergo relative motion along their common boundary, as ζ_A accelerates (Tordesillas et al. 2021a). The change point t_{1b}^* improves on earlier work using a pattern mining approach which detects the time of imminent failure to be one to two hours later: $t = 3,350 = 14:53$ 14 June (Das & Tordesillas 2019) and $t = 3,333 = 13:16$ 14 June (Singh & Tordesillas 2020).

Results from SSSAFE-INV for $t \geq t_{1b}^*$ corroborate the above spatiotemporal dynamics. As seen in Figure 3e, there is a linear decrease with time in the inverse mean velocity of ζ_A from t_{1b}^* , with a high goodness-of-fit as measured by the coefficient of determination R^2 . Note here that Δ is the actual time of failure t_1^F minus the predicted time of failure from the SSSAFE-INV analysis. For reference, and in keeping with the current practice of a pixel-based INV analysis, we also include the results from analysis of the velocity of pixel \wp in ζ_A where the highest velocity at the time of failure was recorded (Figure 3f). The linear regression fits from the three selected time windows serve to illustrate this procedure. That said, we envisage that the implementation of SSSAFE-INV in practical early warning systems would involve the use of rolling and overlapping time windows, since this process allows for continuous updates in the prediction of t^F with every updated data on slope displacement.

Finally, the mechanisms outlined above have been observed in laboratory samples where data on force measurements exist (Tordesillas et al. 2020a, 2020b, 2021a). In all of these cases, SSSAFE accurately captured the complex stress reconfigurations. Competing cracks interact through stress redistribution along redundant force pathways between the recurring bottleneck \mathcal{B} , where the macrocrack that leads to catastrophic failure ultimately forms, and the competing bottleneck, where the crack that undergoes structural arrest (self-stabilise) develops. This interaction between coexisting bottlenecks in PFR continues until all such paths are exhausted, from which time β remains fixed and primed for uncontrolled crack propagation (i.e. previously disconnected microcracks coalesce). Thus, the ultimate effect of stress redistributions along redundant paths is to delay failure, since any damage to the bottleneck leads to a reduction in the system's resistance to failure R^* . However, there is an undesired concomitant which is the considerable uncertainty these stress redistributions present to traditional methods on failure prediction. Unlike SSSAFE, most, if not all these methods do not account for the coupled evolution of damage and force transmission, and generally rely on areas deemed to be experiencing the highest stresses for clues on the location of impending failure. As shown here for the case of Mine 1 and prior studies of other granular systems, this can be misleading in the early stages of PFR because it is during this period that the system embodies redundant force pathways that enable damage to be rerouted and concentrated elsewhere—away from the region of impending failure (Tordesillas et al. 2020a, 2020b, 2021a).

3.2 Mine 2

3.2.1 Background and data on Mine 2

Mine 2 is a rock slope of an open cut mine dominated by intact igneous rock that is heavily structured or faulted by many naturally occurring discontinuities (Figure 4a). An SSR scanned the section of the rock face for displacement for approximately six days from 15:39 19 August, until 07:05 25 August, each scan taking approximately six minutes, again with millimetric precision. Measurements at 5,394 pixel locations were taken every six minutes giving high spatial and temporal resolution for the entire domain, measuring 1,280 m wide and around 224 m high. A rockslide occurred on the southern wall at 03:00 25 August; we refer to this

as the time of failure t_2^F for the rest of this paper. The area that failed, measuring approximately 135 m wide and 145 m high, moved over one million tonnes of debris. Mine 2 reached peak pixel velocity of 2.8 m/day, which is classified as rapid (Cruden & Varnes 1996).

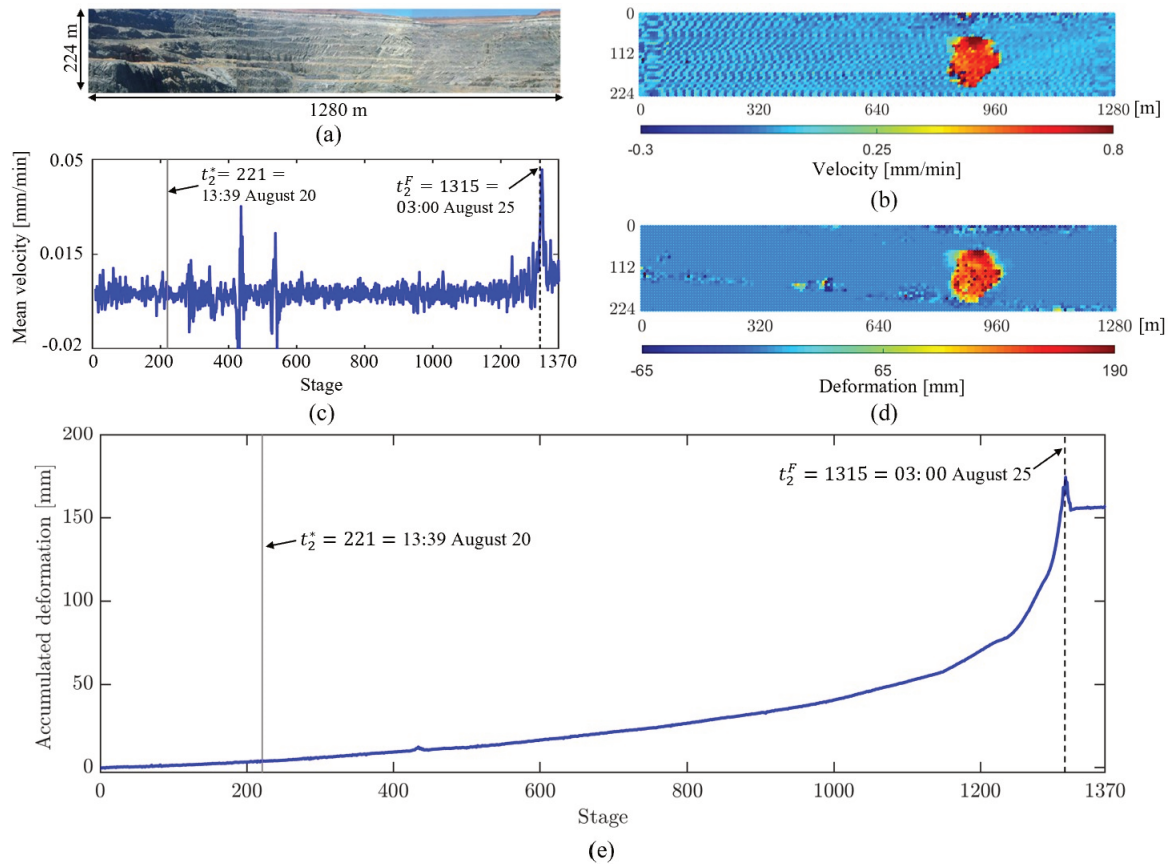


Figure 4 Mine 2: (a) The monitored domain; (b) Spatial map of velocity at time of failure; (c) Time evolution of global mean velocity; (d) Spatial map of accumulated displacement at time of failure; (e) Deformation time series for pixel φ : pixel with the highest rate of movement in ζ_A at the time of failure. Vertical lines mark the regime change point (solid grey line) and the time of failure (dashed black line), respectively

3.2.2 Results on Mine 2

A continual shift in the location of the bottleneck can be observed on the first day of the monitoring period, $1 \leq t < 221$, while the slope's failure resistance R^* decreased (Figures 5a and 5b). On the other hand, trends in both NMI and the Silhouette score S suggest that no substantial clustering in the kinematics developed on this day. NMI fluctuated between 0 and 1 while S remained below 0.5 (Figures 5c and 5d). This implies that the system embodies redundant pathways to divert stresses away from the bottleneck β , consistent with its continual shift in location prior to $t = 221$.

In the ensuing period of $221 \leq t \leq 1,370$, however, kinematic clustering develops as evident in the rise in S (Figure 5d). As failure draws near, intra-cluster motions become coherent and near rigid-body, while inter-cluster motions become increasingly separated as the active cluster ζ_A accelerates (Figure 5d). We see these trends are precisely mirrored by the NMI of the clusters (Figure 5c). Note that the slope failure boundary, shown at $t = 221$ in Figure 5a actually appears as early as $t = 104$ and persists up until $t = 178$, which explains the high NMI scores. However, the kinematic clusters undergo a short period of change during $179 \leq t \leq 221$ which may reflect any number of perturbations on the mine site, including blasting. Around the same time period, large fluctuations can also be observed in S . Eventually S flattens out to a value close to 1, indicative of a strong clustered motion. Together, the evidence from R^* , S and NMI marks a regime change point at $t_2^* = 221 = 13:39$ 20 August, which is just over four days prior to the collapse on

$t_2^F = 1,315 = 03:00$ 25 August. Results from the SSSAFE-INV analysis further corroborate the progressive evolution to collapse at t_2^F (Figures 5e and 5f).

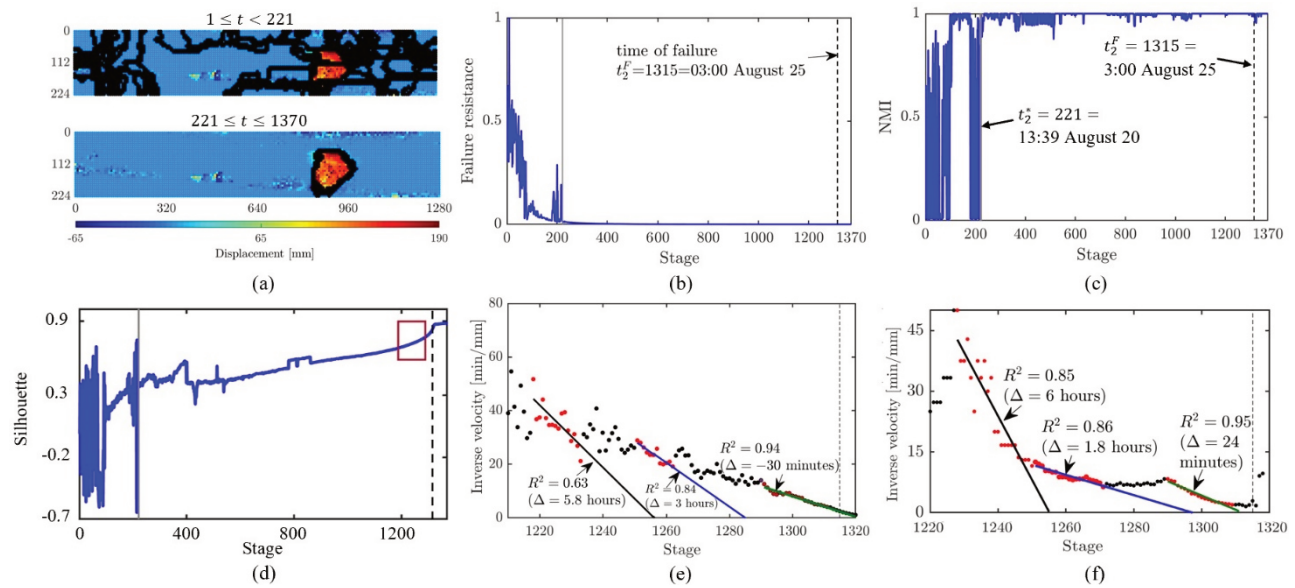


Figure 5 Mine 2: (a) Bottleneck sites across two distinct regimes. Time evolution of (b) failure resistance; (c) NMI; (d) Silhouette S ; (e) Inverse mean velocity of ζ_{A_i} ; (f) Inverse velocity of ϕ . Vertical lines mark the regime change point (solid grey line) and the time of failure (dashed black line), respectively. Red rectangular outline in (d) highlights the time period when SSSAFE-INV analysis was performed. Results of the SSSAFE-INV analysis in (e) and (f) show Δ , the actual time of failure t_2^F minus the predicted time of failure, and R^2 , the goodness-of-fit to the linear regression model

4 Scope and limitation

We have tested SSSAFE for a range of data sets: (a) ductile through to brittle failure in laboratory samples (Tordesillas et al. 2013a, 2015a, 2015b, 2020a, 2020b; Lin & Tordesillas 2014; Kahagalage et al. 2017; Kahagalage 2020), (b) the two mine slopes reported here (see also Tordesillas et al. 2021a), (c) the 2017 Xinmo landslide that led to at least 83 fatalities and buried an entire village in the Sichuan province, China, on 24 June 2017 (Tordesillas et al. 2021a), (d) two separate summit crater rockfalls in Stromboli volcano, Italy on 6–7 August 2014 (Tordesillas et al. 2021b). In all of these cases, the method proposed here gave an accurate prediction of the location of failure.

In general, the method behind SSSAFE works best for high space-time resolution monitoring data and where the monitoring domain covers both stable and unstable areas such that the data is balanced. Like most methods that characterise clustering patterns in data, the predictive capacity of this method suffers and degrades when the input data is severely imbalanced (i.e. the failure zone comprises less than 1% of the total number of monitoring points). Such data imbalances are, however, more likely for regional scale data from space satellite observation systems. In these cases, additional tools are needed such as that discussed in Zhou et al. (2021) which can pinpoint the impending failure locale from an imbalanced data and zoom in on the target area to localise and optimise the deployment of SSSAFE.

Finally, as all SSRs are line-of-sight measurement tools, it is worth noting the implications of angle of incidence of the radar line-of-sight to a failing mass. While the magnitudes of deformation and velocity are affected by the line-of-sight vector loss, the spatial failure boundaries and the relative deformation change (e.g. velocity ratio and acceleration rate) are not affected by line-of-sight vector loss. This is well explained in Section 4.4.3.2 of *Guidelines for Slope Performance Monitoring* (Sharon & Eberhardt 2020). For example, the doubling of a velocity rate for a failure is unaffected by a line-of-sight vector loss from any reasonable radar location; the same can be said for the spatial boundaries of a failure. As a result, SSSAFE remains robust under

different line-of-sight vector loss angles due to the spatiotemporal dynamics of clustering patterns, which rely more on the relative (instead of the absolute) magnitudes of displacements.

5 Conclusion

A holistic framework for SSSAFE is developed. We demonstrate how SSSAFE can be applied to identify emergent kinematic clusters in the early stages of the PFR for two open pit mine slopes using SSR deformation data. The spatiotemporal dynamics of the kinematic clusters reliably predicts where and when catastrophic failure occurs. The clusters share a common boundary along the force bottleneck, the path of least failure resistance. We find a regime change point from which the force bottleneck becomes invariant in space and time through to failure. Simultaneously, intra-cluster (inter-cluster) motions on either side of the bottleneck become very similar or rigid-body (different), as the physical partition induced by the force bottleneck becomes incised in the rock slope. Our findings illuminate a way forward to rationalise and refine decision-making from broad-area coverage monitoring data for improved geotechnical risk assessment and hazard mitigation. To that end, ongoing efforts are focused on the extension of SSSAFE to a probabilistic platform that incorporates uncertainty systematically for various slopes and relevant scenario projections like blasting. Last, this work also highlights an important issue for future studies which may potentially benefit the geotechnical community. This concerns the practical geomechanical manifestation of force chains and force bottlenecks from radar-measured displacements, not just in slope stability analysis, but in other aspects of geotechnical engineering like structural health monitoring. We are exploring these manifestations in a range of soil–structure interaction systems, including retaining walls (Leśniewska et al. 2020).

Acknowledgement

We thank the anonymous reviewers for their constructive comments and suggestions. The two companies who have donated the SSR data for this research, and provided permission for publication on the condition of anonymity, are also gratefully acknowledged.

References

- Ahuja, RK, Magnanti, TL & Orlin, JB 1993, *Network Flows: Theory, Algorithms, and Applications*, Prentice Hall, Hoboken.
- Carlà, T, Intrieri, E, Raspini, F, Bardi, F, Farina, P, Ferretti, A, Colombo, D, Novali, F & Casagli, N 2019, 'Perspectives on the prediction of catastrophic slope failures from satellite INSAR', *Scientific Reports*, vol. 9, no. 1, pp. 1–9.
- Carlà, T, Intrieri, E, Di Traglia, F, Nolesini, T, Gigli, G & Casagli, N 2016, 'Guidelines on the use of inverse velocity method as a tool for setting alarm thresholds and forecasting landslides and structure collapses', *Landslides*, vol. 14, no. 2, pp. 517–534.
- Cruden, D & Varnes, D 1996, 'Landslide types and processes', *Special Report - National Research Council, Transportation Research Board, U.S. National Academy of Sciences*, vol. 247, pp. 36–57.
- Das, S & Tordesillas, A 2019, 'Near real-time characterization of spatio-temporal precursory evolution of a rockslide from radar data: Integrating statistical and machine learning with dynamics of granular failure', *Remote Sensing*, vol. 11, no. 23, p. 2777.
- Dick, GJ, Eberhardt, E, Cabrejo-Liévano, AG, Stead, D & Rose, ND 2015, 'Development of an early-warning time-of-failure analysis methodology for open-pit mine slopes utilizing ground-based slope stability radar monitoring data', *Canadian Geotechnical Journal*, vol. 52, no. 4, pp. 515–529.
- Fukuzono, T 1985, 'A new method for predicting the failure time of a slope', *Proceedings of 4th International Conference and Field Workshop on Landslide*, pp. 145–150.
- Harries, N, Noon, D & Rowley, K 2006, 'Case studies of slope stability radar used in open cut mines', *Stability of Rock Slopes in Open Pit Mining and Civil Engineering Situations*, The South African Institute of Mining and Metallurgy, Johannesburg, pp. 335–342.
- Intrieri, E, Carlà, T & Gigli, G 2019, 'Forecasting the time of failure of landslides at slope-scale: A literature review', *Earth-Science Reviews*, vol. 193, pp. 333–349.
- Kahagalage, S 2020, *A Study of Optimised Network Flows for Prediction of Force Transmission and Crack Propagation in Bonded Granular Media*, PhD thesis, The University of Melbourne, Melbourne.
- Kahagalage, S, Tordesillas, A, Nitka, M & Tejchman, J 2017, 'Of cuts and cracks: data analytics on constrained graphs for early prediction of failure in cementitious materials', *EPJ Web of Conferences*, vol. 140, p. 08012.
- Leśniewska, D, Nitka, M, Tejchman, J & Pietrzak M 2020, 'Contact force network evolution in active earth pressure state of granular materials: photo-elastic tests and DEM', *Granular Matter*, vol. 22, no. 2, pp. 1–31.
- Lin, Q & Tordesillas, A 2014, 'Towards an optimization theory for deforming dense granular materials: minimum cost maximum flow solutions', *Journal of Industrial & Management Optimization*, vol. 10, no. 1, pp. 337–362.
- Rousseeuw, PJ 1987, 'Silhouettes: a graphical aid to the interpretation and validation of cluster analysis', *Journal of Computational and Applied Mathematics*, vol. 20, pp. 53–65.

- Saunders, P, Kabuya, J, Torres, A & Simon, R 2020, 'Post-blast slope stability monitoring with slope stability radar', in PM Dight (ed.), *Proceedings of the 2020 International Symposium on Slope Stability in Open Pit Mining and Civil Engineering*, Australian Centre for Geomechanics, Perth, pp. 507–522.
- Sharon, R, & Eberhardt, E 2020, *Guidelines for Slope Performance Monitoring*, CSIRO Publishing, Clayton, <https://dx.doi.org/10.1071/9781486311002>
- Sullivan, TD 2007, 'Hydromechanical coupling and pit slope movements', Y Potvin (ed.), *Proceedings of the 2007 International Symposium on Rock Slope Stability in Open Pit Mining and Civil Engineering*, Australian Centre for Geomechanics, Perth, pp. 3–47.
- Singh, K & Tordesillas, A 2020, 'Spatiotemporal evolution of a landslide: A transition to explosive percolation', *Entropy*, vol. 22, no. 1, p. 67.
- Tordesillas, A 2018, *Directing Transmission Patterns in Granular Structures from the Grain Scale*, US Air Force Office of Scientific Research Final Report AOARD TA101161 / GL080099.
- Tordesillas, A, Cramer, A & Walker, DM 2013a, 'Minimum cut and shear bands', *Powders and Grains 2013: Proceedings of the 7th International Conference on Micromechanics of Granular Media*, AIP Publishing, Melville, pp. 507–510.
- Tordesillas, A, Walker, DM, Andò, E & Viggiani, G 2013b, 'Revisiting localized deformation in sand with complex systems', *Proceedings of the Royal Society A: Mathematical, Physical and Engineering Sciences*, vol. 469, no. 2152, p. 20120606.
- Tordesillas, A, Kahagalage, S, Ras, C, Nitka, M & Tejchman, J 2020a, 'Early prediction of macrocrack location in concrete, rocks and other granular composite materials', *Scientific Reports*, vol. 10, no. 1, pp. 1–16.
- Tordesillas, A, Kahagalage, S, Ras, C, Nitka, M & Tejchman, J 2020b, 'Coupled evolution of preferential paths for force and damage in the pre-failure regime in disordered and heterogeneous, quasi-brittle granular materials', *Frontiers in Materials*, vol. 7, pp. 1–20.
- Tordesillas, A, Pucilowski, S, Lin, Q, Peters, JF & Behringer, RP 2016, 'Granular vortices: identification, characterization and conditions for the localization of deformation', *Journal of the Mechanics and Physics of Solids*, vol. 90, pp. 215–241.
- Tordesillas, A, Pucilowski, S, Sibille, L, Nicot, F & Darve, F 2012, 'Multiscale characterisation of diffuse granular failure', *Philosophical Magazine*, vol. 92, no. 36, pp. 4547–4587.
- Tordesillas, A, Tobin, S, Cil, M, Alshibli, K & Behringer, RP 2015b, 'Network flow model of force transmission in unbonded and bonded granular media', *Physical Review E*, vol. 91, no. 6, p. 062204.
- Tordesillas, A, Kahagalage, S, Campbell, L, Bellett, P, Intrieri, E & Batterham, R 2021a, 'Spatiotemporal slope stability analytics for failure estimation (SSSAFE): linking radar data to the fundamental dynamics of granular failure', *Scientific Reports*, vol. 11, no. 1, pp. 1–18.
- Tordesillas, A, Zhou, S, Kahagalage, S, Intrieri, E, Nolesini, T & Di Traglia, F 2021b, 'Connecting force chains with fracture paths to forecast crater-rim collapse at active 2 volcanoes: Stromboli August 2014 collapses', in preparation.
- Tordesillas, A, Pucilowski, S, Tobin, S, Kuhn, MR, Andò, E, Viggiani, G, Druckrey, A & Alshibli, K 2015a, 'Shear bands as bottlenecks in force transmission', *Europhysics Letters*, vol. 110, no. 5, p. 58005.
- Vinh, NX, Epps, J & Bailey, J 2010, 'Information theoretic measures for clusterings comparison: Variants, properties, normalization and correction for chance', *The Journal of Machine Learning Research*, vol. 11, pp. 2837–2854.
- Wang, H, Qian, G & Tordesillas, A 2020, 'Modeling big spatio-temporal geo-hazards data for forecasting by error-correction cointegration and dimension-reduction', *Spatial Statistics*, vol. 32, p. 100432.
- Zhou, S, Bondell, H, Tordesillas, A, Rubinstein, BIP & Bailey, J 2020, 'Early identification of an impending rockslide location via a spatially-aided gaussian mixture model', *Annals of Applied Statistics*, vol. 14, no. 2, pp. 977–992.
- Zhou, S, Tordesillas, A, Intrieri, E, Di Traglia, F & Catani, F 2021, 'Pinpointing early signs of impending slope failures from space', *Journal of Geophysical Research: Solid Earth*, in review.